Proceedings of the 21st ICSMGE, Vienna, Austria, 14 – 19 June 2026. Pistrol, Adam & Schweiger (eds.)
Published by: ÖGG, Austrian Society for Geomechanics, Salzburg, Austria, ISBN 978-3-9503898-4-5
https://doi.org/10.53243/ICSMGE2026-2332

Numerical stability evaluation using spectral radius against soil-water coupled analysis based on ***u*-*p*/*u*-*w*-*p*** formulation

Tomohiro Toyoda
Department of civil and environmental engineering, Nagoya University, Japan, toyoda@civil.nagoya-u.ac.jp

ABSTRACT: In this study, we investigated the numerical stability of the soil-water coupling analysis based on the ***u*-*p*/*u*-*w*-*p*** formulations using the spectral radius of the simultaneous recursive equation consisting of the discretized governing equation of ***u*-*p*/*u*-*w*-*p*** and the time integration formulas of Wilson's θ method. Main findings are as follows: 1) The "band-shaped" unstable region of ***u*-*p*** on the permeability coefficient k-time increment Δt plane was investigated. The band bends at the threshold line where the eigenfunction of the main mode of the ***u*-*p*** theoretical solution transitions from exponential (overdamped) to trigonometric (damped oscillation). Therefore, the numerical stability of the step update in the ***u*-*p*** analysis depends on $k/\Delta t$ in the low permeability cases and Δt in the high permeability cases. It is also suggested that the bending of the unstable region is not caused by switching of divergent modes, but by rotation of eigenvectors. 2) the existing criteria for judging applicability of ***u*-*p*** depending on $k/\Delta t$ is generally valid only in the low permeability cases. 3) The most unstable mode in the unstable region of ***u*-*p*** is accompanied by i) stepwise sign inversion of pore water pressure and ii) checkerboard pattern of pore water pressure distribution. The features, i) and ii) are typical phenomena that occur when ***u*-*p*** exhibits instability. The numerical divergence of the ***u*-*p*** solution is characterized by the fact that only the pore water pressure diverges without accompanying soil deformation in the low permeability cases, while the pore water pressure diverges accompanying soil deformation in the high permeability cases. 4) The ***u*-*w*-*p*** is numerically stable regardless of k and Δt (effectiveness of ***u*-*w*-*p***).

KEYWORDS: Soil-water coupling, numerical instability, ***u*-*p*** formulation, ***u*-*w*-*p*** formulation, highly permeable soil

1 INTRODUCTION

The history of "porous media theory," which regards saturated soil as a two-phase mixture, goes back to Fillunger (1913), before Terzaghi proposed the effective stress principle in 1923, Fillunger (1936) formulated the interaction between solids and fluids, and Biot combined solid elasticity theory and permeability theory to give a theoretical explanation from multi-dimensional consolidation (Biot, 1941) to wave propagation (Biot, 1962) in porous media, formed the basis of modern soil mechanics. In the 1980s and 1990s, the "soil-water coupling analysis" was established as typified by the works of Zienkiewicz et al. (1980, 1999) and Verruijt (2010), and is still widely applied in both static and dynamic analyses. Especially, the ***u*-*p*** formulation (hereinafter, referred to as ***u*-*p***), which assumes static seepage of pore water (i.e., the relative acceleration of pore water to the soil skeleton is sufficiently small compared to the acceleration of the soil skeleton), has been widely applied to both static and dynamic analyses. On the other hand, the dynamic motion of pore water is neglected, and the solution of the discretized equation of ***u*-*p*** diverges numerically when applied to problems in which pore water can migrate dynamically, such as coupled problems in highly permeable soils due to the failure of the assumption of static seepage (limitation of ***u*-*p***; Kato, 1995; Noda et al., 2008). The author have developed an analytical method based on the full formulation (***u*-*w*-*p*** formulation, hereinafter, referred to as ***u*-*w*-*p***) that solves the governing equations of the soil-water coupling problem including the equation of motion of pore water without introducing the assumption of static seepage and have demonstrated the effectiveness of this method (Noda and Toyoda, 2019).

In this paper, the numerical stability of the soil-water coupling analyses (***u*-*p***, ***u*-*w*-*p***) are evaluated using the spectral radius of a simultaneous recursive equation constructed from the discretized governing equation. The following contents are included in this manuscript: 1) visualization of the stable range of the ***u*-*p*** soil-water coupling analysis, 2) discussion on of the existing criteria for checking applicability of ***u*-*p***, 3) investigation on the characteristics of diverging eigenmodes in the ***u*-*p*** solution, and 4) demonstration of the validity (unconditional stability) of ***u*-*w*-*p***.

2 GOVERNING EQUATION AND METHOD FOR EVALUATING NUMERICAL STABILITY

2.1 *Governing equations of soil-water coupling problem and their simultaneous recursive equations*

The governing equation based on ***u*-*w*-*p*** for the soil-water coupling analysis using the updated Lagrangian method is shown below (Noda and Toyoda, 2019):

Equation of motion of mixture

$$\rho_s \mathrm{D}_s^2 \boldsymbol{v}_s + \rho_f \mathrm{D}_s \mathrm{D}_f \boldsymbol{v}_f + \rho^f (\operatorname{div} \boldsymbol{v}_s)(\mathrm{D}_s \boldsymbol{v}_s - \boldsymbol{b}) = \operatorname{div}(\mathrm{D}_s \boldsymbol{S}_t), \tag{1}$$

Equation of motion of fluid phase

$$\rho^f \mathrm{D}_f \boldsymbol{v}_f = -\gamma_w \operatorname{grad} h - \frac{\gamma_w}{k} \boldsymbol{w}, \tag{2}$$

Soil-water coupling equation

$$\operatorname{div} \boldsymbol{v}_s + \operatorname{div} \boldsymbol{w} = 0, \tag{3}$$

where ρ, ρ_s, ρ_f, and ρ^f are densities of mixture, solid phase, fluid phase and pore water, respectively. D_s and D_f are the material-time derivatives with respect to the solid and fluid phases, respectively. $\boldsymbol{v}_s$ and $\boldsymbol{v}_f$ denote velocities of solid and fluid phases, respectively, $\boldsymbol{w} = n(\boldsymbol{v}_f - \boldsymbol{v}_s)$ is the averaged relative flow rate of pore water, $\boldsymbol{b}$ is the body force vector per mass, $\mathrm{D}_s \boldsymbol{S}_t$ is the nominal stress rate tensor, $h = z + p/\gamma_w$ is the total head, p is pore water pressure, z is elevation, n is porosity, k is the coefficient of permeability, γ_w is the unit weight of water. On the other hand, the governing equation for ***u*-*p*** is derived by contracting Eqs. (1) – (3) by assuming the seepage acceleration (the relative acceleration of pore water to the soil skeleton) is sufficiently small compared to the acceleration of the soil skeleton ($\mathrm{D}_f \boldsymbol{v}_f - \mathrm{D}_s \boldsymbol{v}_s \ll \mathrm{D}_s \boldsymbol{v}_s$).

Equation of motion of mixture

$$\rho \mathrm{D}_s^2 \boldsymbol{v}_s + \rho^f (\operatorname{div} \boldsymbol{v}_s)(\mathrm{D}_s \boldsymbol{v}_s - \boldsymbol{b}) = \operatorname{div}(\mathrm{D}_s \boldsymbol{S}_t), \tag{4}$$

Soil-water coupling equation

$$\frac{\rho^f k}{\gamma_w} \operatorname{div}(\mathrm{D}_s \boldsymbol{v}_s) - \operatorname{div} \boldsymbol{v}_s + \operatorname{div}(k \operatorname{grad} h) = 0. \tag{5}$$

To discuss $\boldsymbol{u}$-p-induced numerical instability, we assumed infinitesimal elastic deformation that does not cause instability due to material and geometric nonlinearities. Equations (4) and (5) are non-dimensionalized under one-dimensional conditions (Toyoda and Noda, 2021) and then spatially discretized based on the finite element method with Christian and Tamura's methods, following Noda et al. (2008) and Noda and Toyoda (2019). Then, combining the discretized governing equation with the time integration formula of the Wilson-θ method, the system of equations can be summarized into the following algebraic equations.

Spatially discretized time integration formulas & Wilson-θ interpolation formulas

$$\mathrm{A}\boldsymbol{u}_{n+\theta} = \mathrm{B}\boldsymbol{u}_n, \tag{6}$$

Retraction formula for the Wilson-θ method

$$\boldsymbol{u}_{n+1} = \mathrm{C}\boldsymbol{u}_n + \mathrm{D}\boldsymbol{u}_{n+\theta}, \tag{7}$$

where $\boldsymbol{u}_n$, $\boldsymbol{u}_{n+1}$, $\boldsymbol{u}_{n+\theta}$ are coefficient vectors consisting of components of the unknown variables for each degree of freedom at the n-th, (n+1)-th, and (n+θ)-th time step, respectively (n = 0, 1, ...). Specific form of the matrices A to D are omitted due to the space limitation, but they are constant coefficient matrices when assuming infinitesimal elastic deformation. Substituting Equation (6) into Equation (7) and eliminating $\boldsymbol{u}_{n+\theta}$, the following simultaneous recursive equation is obtained.

$$\boldsymbol{u}_{n+1} = \mathrm{E}\boldsymbol{u}_n, \qquad \mathrm{E} = \mathrm{C} + \mathrm{D}\mathrm{A}^{-1}\mathrm{B}. \tag{8}$$

Equation (8) is an update formula to estimate the state at the next step $\boldsymbol{u}_{n+1}$ from the current state $\boldsymbol{u}_n$. If the initial state $\boldsymbol{u}_0$ is given and Equation (8) is applied sequentially, a time history analysis can be performed to conduct the sequential estimation of $\boldsymbol{u}_1$, $\boldsymbol{u}_2$, ... one after the other. The general term can be expressed as $\boldsymbol{u}_n = \mathrm{E}^n\boldsymbol{u}_0$.

2.2 *Stability analysis method using spectral radius*

The eigenvalue problem for the state update matrix E (real asymmetric and diagonalizable matrix) in Equation (8) is defined as follows:

$$\mathrm{E}\boldsymbol{p}_i = \lambda_i\boldsymbol{p}_i \ (i = 1,2,\cdots N), \qquad \mathrm{E} = \mathrm{P}^{-1}\Lambda\mathrm{P}, \tag{9}$$

where N is the total number of degree of freedom, λ_i and $\boldsymbol{p}_i$ (i = 1, 2, ..., N) are the eigenvalue and eigenvectors of E, $\Lambda = \mathrm{diag}(\lambda_1, \lambda_2, \cdots, \lambda_N)$ is the diagonal matrix, and $\mathrm{P} = [\boldsymbol{p}_1, \boldsymbol{p}_2, \cdots, \boldsymbol{p}_N]$ is the diagonalization matrix. The eigenvectors $\boldsymbol{p}_1, \boldsymbol{p}_2, \cdots, \boldsymbol{p}_N$ are all normalized by 2-norm. In this case, the general term $\boldsymbol{u}_n$ is multiplied by using the diagonal matrix Λ of E as follows:

$$\boldsymbol{u}_n = \mathrm{E}^n\boldsymbol{u}_0, \qquad \mathrm{E}^n = \mathrm{P}^{-1}\Lambda^n\mathrm{P}. \tag{10}$$

Furthermore, decomposing the initial state vector $\boldsymbol{u}_0$ into a sum of eigenvectors, $\boldsymbol{u}_0 = \boldsymbol{b}_1 + \boldsymbol{b}_2 + \cdots + \boldsymbol{b}_N$ (direct sum decomposition; $\boldsymbol{b}_j$ is the $\boldsymbol{p}_j$ direction component of $\boldsymbol{u}_0$, j = 1, 2, ..., N), the general term $\boldsymbol{u}_n$ is expressed as

$$\boldsymbol{u}_n = \lambda_1^n\boldsymbol{b}_1 + \lambda_2^n\boldsymbol{b}_2 + \cdots + \lambda_N^n\boldsymbol{b}_N. \tag{11}$$

Therefore, the convergence of Equation (8) (i.e., the vector $\boldsymbol{u}_n$ converges at $n \to \infty$ for any $\boldsymbol{u}_0$ in Equation (11)) is ensured if the absolute values of all eigenvalues should not exceed 1. Thus, defining the spectral radius of E as

$$\rho(\mathrm{E}) = \max(|\lambda_1|, |\lambda_2|, \cdots, |\lambda_N|) \tag{12}$$

the convergence condition of Equation (8) can be expressed as

$$\rho(\mathrm{E}) \le 1 \implies \text{Stable.} \tag{13}$$

3 ANALYSIS RESULTS ($\boldsymbol{u}$-p)

3.1 *Numerical stability of $\boldsymbol{u}$-p*

In order to investigate the stability region of $\boldsymbol{u}$-p, we investigated how the value of the spectral radius $\rho(\mathrm{E})$ of the state update matrix E in Eq. (8) varies with permeability k and time increment Δt. The number of element divisions was set to m = 10 (it was confirmed that further increase of m did not affect numerical stability), and typical parameters were set as θ = 1.4, one-dimensional layer thickness H = 1 m, Young's modulus E = 104 kPa, Poisson's ratio ν = 0.30, soil particle specific gravity G_s = 2.65, and pore ratio e = 1.0. The lower end of the domain was set as a fixed-displacement, undrained boundary, and the upper end as a free-displacement, drained boundary. The eigenvalue analysis was performed using the Intel® Math Kernel Library.

The spectral radius $\rho(\mathrm{E})$ values are plotted on the permeability k – time increment Δt plane in Figure 1. In Figure 1(a), the mountainous distribution of $\rho(\mathrm{E})$ has been confirmed. Binarization of $\rho(\mathrm{E})$ by 1.0+δ (δ: sufficiently small value, here 10^{-4}) yields Figure 2, where the stable and unstable regions of $\boldsymbol{u}$-p are indicated by green and light green, respectively. The figure shows that the unstable region of $\boldsymbol{u}$-p (light green) is distributed in a band, but that it is clearly bent at the center of the figure. In the lower part of the figure (low permeability region, region (I)), the boundary between the stable and unstable zones is obliquely distributed, and therefore, the calculation is determined by the hydraulic conductivity-time increment ratio $k/\Delta t$. However, in the upper part of the figure (high permeability region, region (II)), the boundary is vertically distributed, and therefore, the calculation is not determined by the time increment Δt. The upper area (the high permeability area, area (II) in the figure) is vertically distributed. Besides, the region (III) on the left side of the unstable region exhibits "stable," but this is due to the fact that the time step width is extremely small ($\Delta t < 10^{-8}$ sec), resulting in almost no deformation at each step, and since it takes a huge number of steps to solve the phenomenon, it can be regarded as a region where $\boldsymbol{u}$-p is practically inapplicable. Besides, the appearance of the band-shaped instability region has also been confirmed when using the Newmark-β method instead of the Wilson-θ method as a time-integral formula, but the details are omitted due to the space limitation.

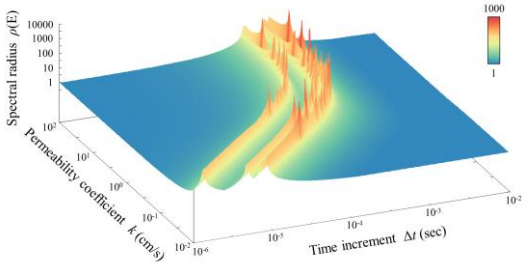

(a) Distribution of spectral radius.

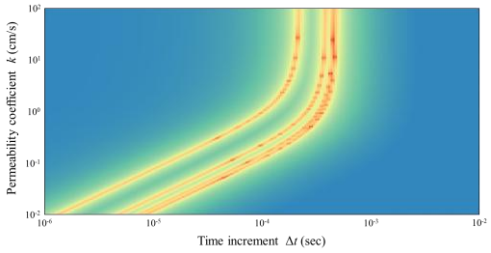

(b) Colormap of spectral radius.

Figure 1. Distribution of spectral radius on k – Δt plane.

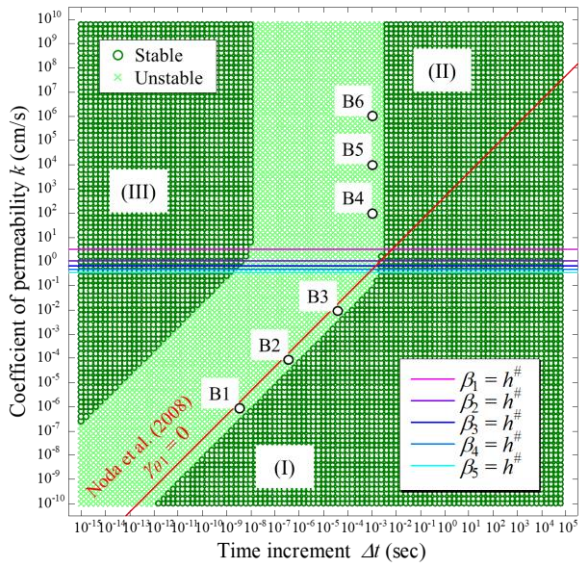

Figure 2. Stable/unstable range of ***u*-*p*** on $k - \Delta t$ plane.

3.2 *Validity of existing criteria for judging applicability of* ***u*-*p***

For the numerical stability of ***u*-*p***, Kato (1995) combined the Routh-Hurwitz stability criterion with the Newmark-β method and proposed the criterion:

$$\epsilon > \frac{k}{g\Delta t} \implies \text{Stable.} \tag{14}$$

Noda et al. (2008) focused on Eq. (5) discretized by the Wilson-θ method, which assumes linearity of "jerk" term (material-time derivative of acceleration), and proposed the following criterion from the physical meaning of the soil-water coupling equation.

$$\gamma_{\theta 1} = \frac{1}{6} - \frac{1}{2\theta\Delta t}\frac{\rho^f k}{\gamma_w} > \frac{k}{g\Delta t} \implies \text{Stable.} \tag{15}$$

Both Equations (14) and (15) suggest that the numerical stability of ***u*-*p*** is determined by $k/\Delta t$. Figure 2 shows the threshold line derived from Equation (15) (red line; the lower part is the stable region), which agrees to some extent with the threshold line obtained from the spectral radius in the low permeability region, but is completely different in the high permeability region. From the above, it can be said that the previous ***u*-*p*** criterion based on $k/\Delta t$ is generally valid only in the low permeability region.

3.3 *Reason why the unstable region bends*

Next, we discuss the reason why the unstable region in Figure 2 bends. According to Toyoda and Noda (2024), the ***u*-*p*** theoretical solution of the time history of dynamic one-dimensional deformation of a saturated elastic column is expressed as a superposition of the eigenfunctions, each of which varies with the coefficient of permeability. If the permeability is small, the eigenfunctions are overdamped (exponential function), but if the permeability is large, they are underdamped (trigonometric function). The $\beta_j = h^{\#}$ line (j = 1, 2, ...) shown in Figure 2 is a threshold line such that the j-th eigenfunction exhibits overdamping below it and underdamping above it. The $\beta_1 = h^{\#}$ line (pink) is particularly important because the displacement time history below it is almost "static consolidation" because the lower eigenfunctions governing the phenomenon are overdamped, but above it, the displacement time history is "damped oscillations" because all eigenfunctions are underdamped, which significantly changes the nature of the solution. Interestingly, the location of the $\beta_1 = h^{\#}$ line coincides with the location of the bending of the ***u*-*p*** instability region estimated from the spectral radius. We hypothesized that the reason for the bending was caused by the difference in diverging eigenmodes.

Table 1 shows the eigenvalues λ_1 of the mode with the largest absolute value of eigenvalues in matrix E (hereafter called the "most unstable mode") for the conditions B1–B3 and B4–B6 located below and above the $\beta_1 = h^{\#}$ line, respectively, in the unstable region in Figure 2. Figures 3 compares the eigenvector $\boldsymbol{p}_1$ components at B1–B6. Table 1 shows that the eigenvalues of B1–B3, which have the same value of $k/\Delta t$ below the $\beta_1 = h^{\#}$ line, are identical, and the components of the eigenvectors shown in Figure 3 are also identical (coaxial), indicating that B1–B3 have identical diverging eigenmodes. Similarly, the eigenvalues and eigenvector components of B4–B6, which have the same value of Δt on the $\beta_1 = h^{\#}$ line, are also identical, indicating that B4–B6 also have the same diverging eigenmodes. Although at first glance it appears that switching of the diverging eigenmode occurs near the $\beta_1 = h^{\#}$ line, the transition of spectral radius (absolute values of eigenvalues of most unstable modes) in the vicinity of the bend in Figure 1(b) is actually smooth without a sharp edge of the bend, indicating that the bend is not caused by discontinuous mode switching, but rather by a continuous transience (rotation) of the the eigenvector of the unstable eigenmode.

3.4 *Features of the diverging eigenmode*

As for the time history of the most unstable mode, Table 1 shows that the eigenvalues of the most unstable modes are all real and negative. This means that (A) the eigenvector $\boldsymbol{b}_1$ of the most unstable mode in the initial state $\boldsymbol{u}_0$ diverges with a "sign inversion at each step" (c.f. divergence of a geometric series with a negative common ratio). As for the spatial distribution of the most unstable mode, (B) pore water pressure at an element is distributed with the opposite sign of the water pressure at adjacent elements as shown in Figure 4 (for the case B2), thus a color map of pore water pressure distribution exhibits a so-called "checkerboard pattern." Both (A) and (B) are typical phenomena that occur when the ***u*-*p*** calculation becomes unstable.

Table 1. Eigenvalue of the most unstable mode.

	Permeability coefficient k (cm/s)	Time increment Δt (s)	$k/\Delta t$ (cm/s)	Eigenvalue λ_1
B1	$10^{-6.0}$	$10^{-8.5}$	$10^{2.5}$	–1.69
B2	$10^{-4.0}$	$10^{-6.5}$	$10^{2.5}$	–1.69
B3	$10^{-2.0}$	$10^{-4.5}$	$10^{2.5}$	–1.69
B4	$10^{2.0}$	$10^{-3.0}$	$10^{5.0}$	–2.09
B5	$10^{4.0}$	$10^{-3.0}$	$10^{7.0}$	–2.09
B6	$10^{6.0}$	$10^{-3.0}$	$10^{9.0}$	–2.09

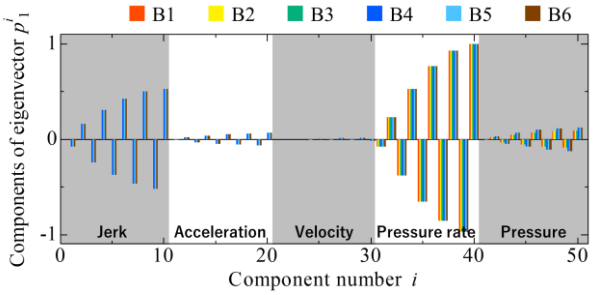

Figure 3. Eigenvector components of the most unstable mode.

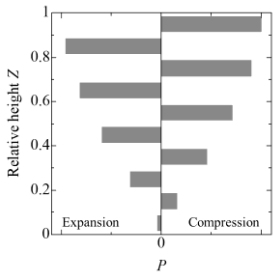

Figure 4. Pore water pressure distribution of the most unstable mode

On the other hand, the direction of eigenvectors (divergence aspect) of the most unstable mode shown in Figure 3 is completely different between B1–B3 and B4–B6. Comparing B1–B3 and B4–B6, the eigenvectors of B1–B3 (low permeability region) contain almost no components related to displacement of the soil skeleton (jerk, acceleration and velocity components), and numerical divergence occurs significantly just in the pore water pressure field and is not accompanied by divergence in the solid deformation field, whereas those of B4–B6 (high permeability region) include significant components related to the displacement of the soil skeleton, and thus diverge is not only in the water pressure field but also with oscillations in the solid displacement field.

4 ANALYSIS RESULTS (***u*-*w*-*p***)

Applying the numerical stability analysis using spectral radius to the governing equations of ***u*-*w*-*p*** (Equations (1)–(3)) and plotting the stability region on the $k-\Delta t$ plane, Figure 5 is obtained. The figure shows that ***u*-*w*-*p*** is stable regardless of coefficient of permeability k and time increment Δt, indicating that ***u*-*w*-*p*** can be used to continue calculations even in regions where ***u*-*p*** is not applicable. Thus, the ***u*-*w*-*p*** is effective for solving highly-permeable soils with large k as well as the instability problems requiring small Δt for capturing phenomena.

5 CONCLUSION

In this paper, we evaluated the numerical stability of the dynamic soil-water coupling equations constructed by combining the time integration formula with the ***u*-*p*** and ***u*-*w*-*p*** discretizations, using the spectral radius, and obtained the following findings.

- The unstable region of ***u*-*p*** exhibits band-shaped distribution on the coefficient of permeability k – time increment Δt plane and it bends at the threshold line where the eigenfunction of the main mode of the ***u*-*p*** theoretical solution changes from exponential (overdamped) to trigonometric (damped oscillation). Therefore, the numerical stability of the step update in the ***u*-*p*** analysis depends on $k/\Delta t$ in the low permeability region and Δt in the high permeability region. It is also suggested that the bending in the unstable region is not caused by switching of diverging modes, but by rotation of eigenvectors.
- The most unstable mode in the unstable region of ***u*-*p*** is accompanied by (A) sign reversal of water pressure at each step and (B) checkerboard-like pore water pressure distribution. The features (A) and (B) are typical phenomena that occur when ***u*-*p*** is applied in unstable regions. The numerical divergence of the ***u*-*p*** solution is characterized by the fact that in the low permeability region, only the water pressure diverges with almost no deformation of the soil skeleton, while in the high permeability region, the water pressure diverges with deformation of the soil skeleton.
- The existing $k-\Delta t$-dependent criteria for checking ***u*-*p*** applicability is generally valid only in the low permeability region.
- The ***u*-*w*-*p*** is numerically stable regardless of the hydraulic conductivity k and time interval Δt even at the unstable region of ***u*-*p*** (effectiveness of ***u*-*w*-*p***).

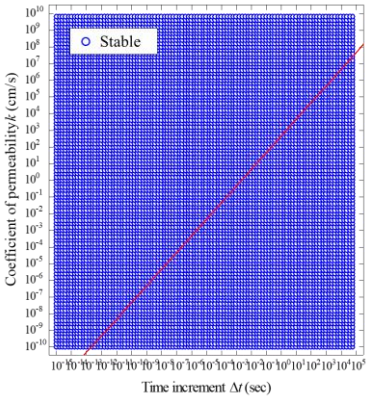

Figure 5. Stable/unstable range of ***u*-*p*** on $k-\Delta t$ plane.

ACKNOWLEDGEMENTS

I would like to thank co-researcher, Prof. Toshihiro Noda (Nagoya University), for his helpful advice in carrying out this research. The research was supported by JSPS Grant-in-Aid for Scientific Research 22K14324.

REFERENCES

Fillunger, P. 1913. Der Auftrieb in Talsperren,österr, *Wochenschrift für den öffentlichen Baudienst*, 532-556, 567-570. (in German)

Fillunger, P. 1936. Erdbaumechanik? Wien: Selbstvrlag des Verfassers. (in German)

Biot, M.A. 1941. General theory of three-dimensional consolidation. *Journal of Applied Physics*, 12, 155-164.

Biot, M.A. 1962. Mechanics of deformation and acoustic propagation in porous media. *Journal of Applied Physics*, 33, 1482-1498.

Zienkiewicz, O. C., Chang, C.T. and Bettess, P. 1980. Drained, undrained, consolidating and dynamic behaviour assumptions in soils, *Géotechnique*, 30(4), 385-395.

Verruijt, A. 2010. Dynamics of Porous Media. In: An Introduction to Soil Dynamics. *Theory and Applications of Transport in Porous Media*, 24, Springer.

Zienkiewicz, O. C., Chan, A.H.C., Pastor, M., Schrefler, B.A. and Shiomi, S. 1999. *Computational Geomechanics with special reference to Earthquake Engineering*, John Wiley &Sons.

Kato, M. 1995. Research on multi-dimensional liquefaction analysis method and its application, Doctoral thesis of Gifu University, 45-53. (in Japanese)

Noda, T., Asaoka, A. and Nakano, M. 2008. Soil-water coupled finite deformation analysis based on a rate-type equation of motion incorporating the SYS Cam-clay model, *Soils and Foundations*, 48(6), 771-790.

Noda, T. and Toyoda, T. 2019. Development and verification of a soil-water coupled finite deformation analysis based on ***u*-*w*-*p*** formulation with fluid convective nonlinearity, *Soils and Foundations*, 59(4), 888-904.

Toyoda, T. and Noda, T. 2021. Numerical simulation based heuristic investigation of inertia-induced phenomena and theoretical solution based verification by the damped wave equation for the dynamic deformation of saturated soil based on the ***u*-*w*-*p*** governing equation, *Soils and Foundations*, 61(2), 352-370.

Toyoda, T. and Noda, T. 2024. Unconditional convergence of theoretical solutions to ***u*-*p*** formulation, *Soils and Foundations*, 64(1), 101421.